This is an unformatted copy of the manuscript, "Modulated photocurrent spectroscopy of CdTe/CdS solar cells– equivalent circuit analysis" by B. H. Hamadani et. al.

This work was published online on 05/20/2013 in the journal, Solar Energy Materials & Solar Cells

116 (2013) 126-134

Direct link:
http://www.sciencedirect.com/science/article/pii/S0927024813001761

Modulated photocurrent spectroscopy of CdTe/CdS solar cells– equivalent circuit analysis

B. H. Hamadani[1,*], J. Roller[1], P. Kounavis[2], N. B. Zhitenev[3], and D. J. Gundlach[4]

[1] *Engineering Laboratory, National Institute of Standards and Technology, Gaithersburg, MD, 20899, USA*

[2] *Department of Engineering Sciences, School of Engineering, University of Patras, 26504 Patras, Greece*

[3] *Center for Nanoscale Science and Technology, National Institute of Standards and Technology, Gaithersburg, MD, 20899, USA*

[4] *Physical Measurement Laboratory, National Institute of Standards and Technology, Gaithersburg, MD, 20899, USA*

Abstract

Modulated photocurrent spectroscopy was used to investigate the dynamic response of charge carrier transport in thin film CdTe/CdS solar cells. The impact of light bias and temperature over a broad excitation frequency range were measured. The observed features of the data, including a photocurrent 'phase-lead' and a 'phase-lag' over different regions of the frequency spectrum, were explored in the context of an equivalent circuit model. Comparisons between the model's predicted performance and the measured data suggest that charge carrier recombination at the cell's back metal/semiconductor contact is the main source of photocurrent loss in these devices.

[*] Corresponding author.
E-mail address: behrang.hamadani@nist.gov

1. Introduction

Thin film cadmium telluride/cadmium sulfide (CdTe/CdS) solar cells have demonstrated good viability for providing efficient, low-cost and large-area photovoltaic (PV) electricity generation [1]. Further improvements in device performance and long term stability, however, require an improved understanding of the photocurrent loss mechanisms within these devices. A variety of time-resolved and frequency-domain electrical and electro-optical characterization techniques, along with the steady state current-voltage (*I*-*V*) or capacitance-voltage (*C*-*V*) measurements, have been used to gain better insight into device performance. These techniques include impedance (or admittance) spectroscopy [2–7], deep level transient spectroscopy (DLTS) [8], temperature-dependent *I*-*V* and *C*-*V* measurements [9–13], light and voltage bias dependent external quantum efficiency (EQE) measurements [14,15], photocapacitance studies [16], current transient studies [10,17], and a variety of other methods used to explore sub-bandgap defects and impurity states, contact effects, recombination losses, and degradation mechanisms.

Frequency domain ac electrical characterization, such as impedance spectroscopy, has been a popular technique [2–7] to study the influence of majority carrier traps on device performance. For this type of method, a small ac perturbation voltage signal, superimposed on a larger dc bias voltage, is applied to the cell and the resulting current generation is measured by an impedance analyzer or a lock-in amplifier. The impedance of the device as a function of frequency is obtained through amplitude and phase measurements of the current. The appearance of step-like features in the real part of the impedance signal (corresponding to peaks in the imaginary component vs. frequency plots) have traditionally been associated with defect energy levels within the material's band gap. Several distinct trap states have been identified and extensively probed by several research groups [2–5,9]. Recently, the existence of a back-contact barrier at the electrode/CdTe interface was found to manifest itself as a "trap signature" during impedance measurements, yielding activation energies similar to traps observed using other techniques such as DLTS [9,18]. In a separate study of Cu(In,Ga)Se_2 (CIGS) solar cells, the difficulty with interpreting the impedance results in terms of trapping phenomena was raised [19]. The researchers of this study on CIGS cells emphasized the non-trivial influence of a non-Ohmic back-contact on the admittance data. Further detailed *I*-*V* and *C*-*V* measurements and modeling, particularly on stressed devices and cells with different back-contact processing [9,11,12,20–22], have revealed that a non-Ohmic Schottky back-contact can indeed significantly influence the device's performance.

In this paper, the ac photogenerated current response in CdTe/CdS solar cells when subjected to modulated photocurrent spectroscopy (MPCS) [23–31] is reported. Results from tests conducted over a broad temperature and frequency range were collected and studied. To help with understanding the measured performance, an equivalent circuit (EC) model that includes the contribution of a non-Ohmic back contact was formulated. Predictions using a simplified version of this model fit the measured data from tests at or near room temperature very well. With the aid of these comparisons, the photocurrent 'phase-lead' and the 'phase-lag' behaviors that occur over different regions of the frequency spectrum can be explained. The model allows for extraction of the contact resistance and the capacitance. At lower temperatures, additional features that appear in the data can be adequately captured by introducing a slight modification to the basic equivalent circuit model. Overall, the measurements

demonstrate significant charge carrier recombination in the presence of light bias and at lower temperatures. These measurements are consistent with the back flow of minority carriers (electrons) towards the back contact interface within the cell [12], where surface recombination occurs. By adjusting the contact properties, the photocurrent loss due to recombination can be appreciably reduced.

2. Experimental details

For these experiments, commercial-grade CdTe films with typical thickness of 3.5 μm grown on CdS/TCO (transparent conductive oxide)/glass were carefully retrieved from a PV module that had been partitioned into several pieces. The back contact (along with the glass and polymer encapsulants on the back side) was mechanically stripped. Scanning electron microscopy and optical imaging inspection of the exposed films showed no obvious signs of damage to the surface. The exposed films were then cleaned and etched in a bromine/methanol solution[32]. Shortly thereafter, a new back contact was added. The back contact, which consisted of (2 to 3) nm of Cu followed by 50 nm of Au, was deposited using thermal evaporation through a shadow mask having dimensions on the order of a few mm. This process resulted in typical *J-V* parameters of V_{oc} = 0.8 V, J_{sc} = (19 to 20) mA/cm^2, and efficiencies = (8 to 9) % constituting reasonable device performance.

The MPCS measurements, sometimes referred to as intensity modulated photocurrent spectroscopy (IMPS)[25,33,34], were performed using a high-power, 518 nm light emitting diode (LED). This LED was operated by applying a sinusoidal voltage signal at different frequencies. The sinusoidal voltage excitation, which is controlled by a function generator, is first amplified by a custom-designed, high-frequency power amplifier before being applied to the LED. The intensity of the light output from the LED was also adjusted using a neutral density filter. The intensity was measured using a calibrated 80 MHz-bandwidth reference Si photodiode that was placed at approximately the same location as the mounted solar cell during a separate run. Using this approach, the measured photocurrent response from the cell is normalized by the intensity of the light. Consequently, the photo-generated current is reported in units of A/W on all the data plots shown herein.

The typical frequency domain of operation for these experiments was 10 Hz to 1 MHz. Notably, for the low end of this frequency excitation domain – i.e., when approaching the dc limit – the measurement corresponds to the spectral responsivity of the cell at 518 nm. The cell photocurrent was measured by a high bandwidth current preamplifier (200 MHz at the lowest gain) that has a dc bias voltage capability. The input and output impedance of the preamplifier was 50 Ω. The voltage bias capability of the amplifier was used to ensure a predetermined constant voltage across the cell under various levels of illumination intensity. In other words, the operational voltage of the cell under test was not allowed to change with increase in light bias intensity. The amplified current was then fed to a 50 MHz bandwidth lock-in amplifier that was externally synced with the function generator. The light bias source was a high-power white LED operated in dc mode. Both the modulated light and the bias light fully illuminate the total device area (overfill illumination). The entire measurement was controlled by a computer program, with data recorded as a function of frequency. Prior to photocurrent frequency sweeps, the cells were kept in the dark for up to 10 minutes. The ambient room light was always turned

off for the entire duration of the measurement. In between temperature measurements, the cells were kept in darkness. Both the modulated LED light and the light bias LED were water-cooled to prevent unnecessary heating of the sample environment. The light bias was progressively increased from no background light to the values quoted in the figures. Measurements were performed multiple times on variety of samples to make sure the results discussed here are representative. The low temperature tests were performed using a table-mount, He vapor-cooled optical cryostat that allowed testing over the temperature range of 320 K to 100 K.

3. Room temperature measurements

3.1. Observations and trends

MPCS and IMPS measurements have traditionally been used in semiconductor/electrolyte systems to study transfer rates, recombination phenomena and diffusion limited transport [29,33,35]. These measurement methods have also been used for defect spectroscopy and density of state determinations in photoactive semiconductor materials, especially ones fabricated as single layer films with planar contacts [23,26–28,36]. Recently, this technique and a variation of it which includes sub-gap illumination, has been used to study defect states in CIGS solar cells[30,31], and interface recombination in organic photovoltaic devices [34,37]. For the work reported in this paper, by comparison, the MPCS technique was used to study the dynamic response of charge transport in CdTe based solar cells. As a complement to the laboratory study, moreover, an equivalent circuit (EC) analysis was conducted to aid the interpretation of the observed phenomena in the tested CdTe cells.

Figures 1 and 2 show a summary of the room temperature measurements on two typical CdTe devices, one with reasonably good contacts and device performance (Fig. 1), and another with inferior contacts (Fig. 2). Figures 3a and 3b show the corresponding *I-V* curves for these two devices in dark and under illumination by an LED light source. The severe current roll-over at high forward bias for the device with inferior contacts, as seen in Fig. 3b, illustrates how bad the contact formation to the CdTe film is for that device. The inferior device was fabricated by inadequate surface cleaning and a very small thickness of Cu (< 2 nm), whereas the better device received proper surface treatment (wet chemical etch) and a Cu layer thickness of > 3 nm [11,32]. Figures 1a and 2a show the intensity-normalized real part of the measured photocurrent as a function of excitation angular frequency, ω, and figures 1b and 2b show the normalized imaginary component of the photocurrent for several light bias conditions. The modulated light intensity for the device shown in Fig. 1 is approximately 0.32 W/m^2, resulting in a low frequency root-mean-square (rms) photocurrent of $\approx$ 440 nA under no light bias (no LB). The light intensity for the device shown in Fig. 2 is $\approx$ 0.38 W/m^2, resulting in a low frequency $I_{rms} \approx$ 970 nA. The device areas are 4.36 mm^2 and 9.0 mm^2, respectively. The real part of the current in both devices under no LB conditions (sometimes referred to as dark conditions in this paper) exhibit a small characteristic 'step-down' in the frequency range (10 to 20) krad/s, corresponding to a small negative-value dip in the imaginary component of the current. This behavior represents a small phase lag in the photocurrent data with respect to the excitation source. In the Nyquist plot representation, this phase lag corresponds to a small semicircle in the 4th quadrant and can represent a small resistance-capacitance (RC) loss mechanism [29,33]. However, as increasing amounts of light bias are applied to the two devices, the

step-down feature of I_{re} diminishes and gives way to a 'step-up' feature. This step-up corresponds to a phase-lead between the current and the light excitation, and has been associated with charge carrier recombination processes (such as the electrolyte/semiconductor interface) in various photoelectrochemical systems [29,35,38], and more recently in organic solar cells [34,37]. In the Nyquist plots, this phase lead appears as a small semicircle in the 1st quadrant. At higher frequencies, the I_{re} drops towards zero for all devices due to the finite device series resistance. Completely capturing this characteristic was not possible due to limitations of modulating high-powered LEDs at such higher frequencies.

The imaginary and real components of the photocurrent in the frequency domain contain information about the origin of the main loss mechanisms of the cell which could not be achieved by means of other techniques. The MPCS performed on inorganic nanocrystalline materials reveals a photocurrent that usually lags the light intensity which implies that the MPCS measurement is limited by carrier transport. The observed characteristics of the photocurrent of the CdTe device in the low frequency region and under light bias leads the light intensity and produces a positive phase shift, thus giving rise to a small semicircle in the 1st quadrant in the Nyquist plot. This characteristic is the signature of a surface/interface recombination rate, as has been reported for various photoelectrochemical systems [29,35,38] and organic solar cells [34,37]. In addition, the increase in the magnitude of the photocurrent's positive imaginary component with modulation frequency implies successful transport of the carriers, which have escaped geminate recombination, to the interface. Recombination takes place at lower frequencies with carriers being trapped at the surface/interface. Had the geminate recombination loss mechanism been more dominant, only a phase lag would have been expected over the entire frequency range. The separation of the carriers would not have happened and the interfacial charging current would not have been observed.

The peak magnitude of the ac photocurrent in the I_{re} vs. ω plots is known as the generation current and indicates the maximum photocurrent that could be produced by a cell in the absence of any surface/interfacial recombination. The generation current can be compared with the low frequency limit of the real component of the photocurrent, which corresponds to the dc photocurrent that governs the conversion efficiency of the cell. From this comparison, the extent of the effect of interfacial recombination on cell efficiency can be estimated. As shown in Figs. 1 and 2, the maximum generation currents in the two types of cells are systematically slightly higher than the respective low frequency limit of the ac component when light bias is introduced. For the most representative case (i.e., highest light bias), approximately 5 % and 15 % reductions in cell efficiency are noted for the devices with good and inferior contact properties, respectively, due to the surface/interfacial recombination. As is expected, the inferior contacts contribute to comparatively higher rates of surface/interface recombination, which in turn, degrade cell efficiency more. This implies that if the contacts are not very good, dc quantum efficiency under high light bias conditions will show a decrease proportional to the severity of the contact effects and the interfacial recombination caused by the contacts. Therefore, as exhibited by the two test CdTe based solar cells then, the quality of the cell's back contact can limit the efficiency of the cell. Fortunately, the impact can be studied using MPCS.

The excitation frequency at which the photocurrent's positive imaginary component peaks has been related to the rate of decay of photogenerated minority carriers at the surface states and to the interfacial recombination rate. The following equation from Reference 34 provides a convenient way to quantify these observations for the photocurrent spectra as a function of frequency in the cases where a phase-lead is observed:

$$i = g\left(1 - \frac{\gamma}{1+(j\omega\tau)^{\alpha}}\right) \qquad (1)$$

where *g* is the ac generation current, γ is the fraction of charge carriers participating in the interfacial relaxation event, τ is the relaxation time (with $1/\tau = k$, the recombination rate), α is a parameter that accounts for a distribution of relaxation times, and *j* is the imaginary unit. Performing a fit of this equation to the phase-lead curves of Figs 1 and 2 with the highest amounts of light bias (excluding very high frequencies) results in $g \approx 0.29$ A/W, 0.22 A/W , $\gamma \approx 0.05,\ 0.16$, $\tau \approx 5.3\ \mu$s, 8.0 μs , and $\alpha \approx 0.92,\ 0.75$ for the good and inferior-contact devices, respectively. The values of *g* correspond to the peak values of I_{re} vs. ω plots (maximum attainable photocurrent). The γ fractions obtained are consistent with the 5 % and 15 % efficiency reductions estimates, and the τ values suggest a relatively high recombination rate for both samples. The parameter τ is unrelated to the bulk charge carrier lifetimes in CdTe (which are many orders of magnitude lower) because equation 1 is used to analyze the recombination feature of the data associated with contact effects in these samples. Values of α <1 suggest a distribution of relaxation times [34]. In addition, the increase of light bias systematically produces a small increase in the recombination rate. Since this rate is expected to account for the population of the interface state density, it can be concluded that this population presents a small increase with bias light.

3.2. Equivalent circuit model

A simple equivalent circuit model adopted from reference [39], which was originally used to investigate time-resolved photocurrent transients at semiconductor/liquid interfaces, was utilized to help explain the laboratory findings. The model was selected because it accounts for the effects of contact resistance and can predict both the phase-lead and phase-lag behavior observed in the laboratory data. Figure 4a shows a simplified energy band diagram schematic of the CdTe device under the effect of a non-Ohmic back contact [12,40]. The junction region can be represented by a depletion capacitance, C_d, and a parallel resistance, R_p, representing electron-hole recombination within the junction. The contact resistance and capacitance are similarly denoted by R_c and C_c, respectively. These contact properties may be responsible for a back flow of electrons towards the contact, leading to surface recombination of electrons near the metal. This model, as will be discussed in detail below, not only provides an explanation for the recombination loss in these devices under illumination (or at low temperatures), but also allows for extraction of the parameters associated with the contacts.

In the ac domain at room temperature and under the conditions of this experiment which involve photocurrent measurements without an application of an ac voltage, the device can be represented by the EC of Fig. 4b (EC model 1). It is noted that in the ac domain, diodes are modeled as a parallel combination of a voltage-dependent capacitive and a resistive element [12] since this closely mimics the

diode's ac response. A series resistance term, R_s, is added to account for other resistances within the cell, such as the neutral CdTe and CdS resistances plus that of the TCO. The ideal current source, I_0, captures the photocurrent generated by the cell as a result of the excitation light source, and is related to the light intensity. To solve for current, *i* as a function of ω, the impedance of the circuit as seen by the current source is first evaluated: $Z = Z_1.Z_2 / (Z_1 + Z_2)$, where $Z_1 = Z_d.R_p / (Z_d + R_p)$, and $Z_2 = R_s + Z_c.R_c / (Z_c + R_c)$ as shown in Fig. 4b by dotted circles. Furthermore, $Z_d = 1/\ j\omega C_d$, and $Z_c = 1/\ j\omega C_c$. The current *i* through the ammeter A is given by $i = I_0 - (V / Z_d) - (V / R_p)$, where *V* is the voltage drop across C_d or R_p and is given by $V = I_0 Z$. Solving for *i,*

$$i = \frac{I_0 R_p (1 + jC_c R_c \omega)}{R_c + R_p + R_s + j(C_d R_p (R_c + R_s) + C_c R_c (R_p + R_s))\omega - C_c C_d R_c R_p R_s \omega^2} \qquad (2)$$

After obtaining values for the Equation 2 lumped constants that collectively yielded the best fits to the data in Figures 1 and 2, the real and imaginary components of Equation 2 were independently calculated as a function of angular frequency. For the fitting procedures, the values of C_d for each device were previously determined through impedance measurements and kept constant. Even under light bias, the values of C_d were not changed in the modeling because the cell was operated and maintained at reverse bias voltages of -0.2 V for Fig. 1, and -0.4 V for Fig. 2, a regime where the cell was observed to be mostly depleted. The value of I_0, which is only a prefactor that is related to the intensity of the modulated light, was also fixed for each device. The values of I_0 are different for the two test cells and the resulting fits because the measured light intensities were slightly different.

The fits to the two sets of data are shown in Figures 1 and 2, with the fitting parameters listed in Table 1. The simple model captures the overall behavior of the two devices at varying light bias intensities, including the step-up and down features exhibited in the I_{re} plots and the dips and peaks that occur in the I_{im} data. In general, the fit agreement improved with increased light biasing and was better for the cell having the inferior contacts. In the case of the device in Fig. 1 having the better quality contacts, when no light bias is present, the parallel resistance is higher than the contact resistance by more than a factor of 30 (in terms of real parts of impedances, $Z_1/Z_2 \approx$ 400 kΩ / 13 kΩ), hence the internal photocurrent losses are small at low frequencies and the circuit-extracted current is maximized. At the frequency of 60 Krad/s where the step-down feature occurs in the real photocurrent plots, Z_1 has decreased to ≈ 5 kΩ and is very comparable to the contact impedance value, Z_2 ≈ 4 kΩ. This result means that more of the photocurrent will now be lost to the recombination within the device because the contacts do not allow good extraction of charges, thus yielding a decrease or step-down from the low frequency value. The frequency at which this step feature (or the dip in I_{im} plots) takes place depends on the individual values of the resistances and capacitances associated with the contact and the junction. At the highest values of the frequency, the impedance of Z_1 loop is far less than Z_2, and hence the photocurrent measured through the external circuit (A) drops to 0.

The opposite scenario takes place when light bias is progressively applied to the device. It is well known that the parallel resistance in CdTe devices, sometimes referred to as the shunt resistance in dc equivalent circuit models of solar cells, *decreases* significantly under light bias. As shown by the fit

parameters given in Table 1, R_p as well as R_c are significantly reduced under light bias. However, the decrease of R_p with light bias is more significant; even when R_c is not very large, the ratio of Z_1/Z_2 at low frequencies is not very large (≈ 7). Hence, the circuit photocurrent is reduced. At angular frequencies around 600 krad/s, this impedence ratio increases slightly, to approximately 10, which allows for more current extraction in the circuit. This increase appears as the step-up feature in the I_{re} vs. ω plots. A very similar effect takes place with the poorly contacted device of Fig. 2. The results, however, are more pronounced. For example, the low frequency I_{re} data of Fig. 2a (inferior contacts) show a decrease of about 30 % between no light bias and a light bias current of 200 μA, whereas the device of Fig. 1a (good contacts) shows only an 11 % reduction and, at this point, the degradation is observed to saturate. The reason for this difference is that the contact resistance of the Fig. 2 sample (see Table 1) is at least an order of magnitude higher than that of the good device when subjected to a large light bias. This outcome is generally consistent with the behavior of the shunt and series resistances of the devices as determined from the *I-V* curve measurements in the dark and under illumination. For example from Fig. 3a, it is observed that the shunt resistance in the reverse bias region decreases from 150 kΩ in the dark to 40 kΩ under the given illumination, whereas the series resistance as extracted from the V_{bias}>1 V region drops from 1.7 kΩ in the dark to about 200 Ω under light. Similarly, Fig. 3b shows that the shunt resistance of the inferior device drops from 500 kΩ in the dark to 3.7 kΩ in the light (at -0.4 V) and the series resistance decreases from 23 kΩ to 17.9 kΩ under light. These values, although different from the fit values show the trend that smaller shunt to series (contact) resistance ratios correspond to bad *I-V* curves and larger recombination loss. The fit parameters also show that the values of the contact capacitance for the good device are significantly higher than the poorly-contacted cell, which indicates a smaller depletion region (more doping of the contact region) near the metal contact of the good device. Notably, the values of R_p and R_c extracted from these fits are very consistent with those extracted from the dc-limited *I-V* data for the cells when tested in the dark and under a light bias.

One notable difference between the two test samples is the contact capacitance for the good device increased by more than a factor of 2 between the dark state and the maximum light bias state, while the opposite occurred for sample with inferior contacts. Specifically, the capacitance for the cell having the inferior contacts decreased, and by a comparatively large amount (approximately 28 %) between the dark and maximum applied light bias cases. This result seems to indicate a further reduction of the width of the contact depletion region for the good device under illumination (from ≈ 200 nm in the dark to ≈ 72 nm under maximum light bias), but no change or a slight deterioration of the contact properties under light bias for the poorly contacted device (from ≈ 570 nm in the dark to ≈ 800 nm under light bias). In either case, since the value of the parallel resistance is always lower under light bias than in the dark, the low frequency or dc limit of the I_{re} component is always reduced. The data suggests that for devices fabricated with optimum contact properties, i.e., contact resistances of < 5 Ω cm^2, the photocurrent phase-lead signature observed in the lab tests should diminish significantly.

4. Temperature dependent measurements

Temperature dependent measurements were performed on a device with poor contact properties (i.e., a cell having a series resistivity of 2500 Ω cm^2 at near dark conditions as derived from *I-V* data

collected when testing at room temperature) to investigate the effect of the temperature on the different model parameters. Figures 5a-c show the results of these measurements for intensity-normalized I_{re} vs. ω, I_{im} vs. ω, and the Nyquist plots of I_{re} vs. I_{im}, respectively, for the device when subjected to a fixed light bias. As a reference, the test cell produced a dc current of 24 μA when measured at 300 K and exposed to the chosen light bias. Figures 6a-c, in addition, show the temperature data for the same test sample when exposed to no light bias. A dc voltage of -0.1 V was maintained for all measurements on this same test cell.

For the equivalent circuit modeling of these data at all temperatures, the EC model 1 shown in Fig. 4b is no longer sufficient. Additional features appear in the data, particularly at low temperatures and high frequencies that can only be captured by modifying EC 1. The simplest modification that is physically relevant is to add a capacitance element, C_b, (bulk capacitance) in parallel with R_s, followed in series by another purely resistive element R_{ss}. Although the origin of C_b is not clear, it represents an aggregate capacitance that is related to the depletion effects at the grain boundaries of both the CdTe and CdS [41]. The improved equivalent circuit model, shown in Fig. 4c, can be used in a similar fashion as outlined above to solve for the frequency dependent current that flows in the external circuit. The resulting equation was then used to fit the temperature dependent data from ≈ 200 K down to 100 K for the fixed light bias case. By comparison, this improved model was found to model the laboratory data better for the no light bias case for cell temperatures from 250 K to 130 K. For the higher temperature data, for both the fixed light bias and no light bias cases, the EC model 1 was sufficient to capture most of the frequency response. The results of this modeling are shown in Figs. 5 and 6. Table 2 lists the values of the parameters derived and used for this analysis.

Figure 5 demonstrates the very good agreement obtained between the measured data and the proposed models for both the real and imaginary components of the current. EC 1 captures the behavior of the data in the 320 K to 200 K range reasonably well, whereas EC 2 becomes necessary to obtain good agreement at low temperatures (200 K to 100 K) and at the highest frequencies. As T is lowered below room temperature, a significant phase-lead develops, seen as larger positive I_{im} peaks, or larger circles in the first quadrant of the Nyquist plots. This phase lead arises because the contact resistance drops faster than R_p as T is lowered, causing the ratio of the junction to contact impedance to decrease. It should be noted that the C_b and R_{ss} terms that are added in EC model 2 actually do exist at higher temperatures; however, since the value of R_s is very small, their effect is negligible over the examined frequency range. Since R_s shows a temperature-activated behavior, its value is larger at lower temperatures and therefore it becomes necessary to include the two new elements in the model to capture the behavior of the data. In the case of no LB measurements, however, (Fig 6 data), the EC model 2 needs to be applied, even at temperatures as high as 250 K because the value of C_b is relatively large (~10^{-8} F) and so influences the behavior of the I_{re} and I_{im} curves at lower frequencies more than the case with LB. This difference could be related to the influence of the light bias on the depletion of the grain boundaries or the occupancy of traps in the dark vs. under light bias. Furthermore, from Fig. 6, it can be seen that the photocurrent data develop a phase-lead at temperatures below 250 K (small circles in the 1st quadrant in Fig. 6c), which as explained earlier is due to the low ratio of the junction to contact impedance. Even with the revised model, the no LB data cannot be captured very well down to the lowest temperatures. This finding is

particularly evident in Figs. 6b and 6c where the imaginary part shows significant disagreement with the model calculations. The data with light bias are captured well down to the lowest measured temperatures for both components of the current.

Turning to the various fit parameters, some did and others did not exhibit a temperature dependence. The parameter C_d was fixed, for example, its value being previously determined through impedance measurements at the fixed reverse bias voltage of -0.2 V. The parallel resistance parameter, R_p, shows higher values at lower temperatures (although for LB data it was mostly unchanging between 320 K to 200 K), suggesting a turn-off of some recombination channels (possibly a freeze-out of defect-mediated recombination) within the junction as the device is cooled. The parameter R_s, which is likely related to the bulk resistance of CdTe, shows an activated behavior with temperature; although not included here, the plots of Ln(R_s) vs. *1/T* for both the dark and the LB data reveal an activation energy in the range of (0.11 to 0.12) eV over all temperatures. This value is very consistent with the report of temperature activated mobility in CdTe with an activation energy of 0.14 eV [42]. The parameter R_{ss} shows a weak temperature dependence, and could be related to charge conductivity through CdS or the TCO, with an activation energy of 60 to 80 meV. The parameter C_b is almost temperature-independent for the LB data and has relatively small values, but shows a strong temperature dependence for the dark data with large values at higher temperatures. These trends point to the possible influence of both light bias and temperature on the charge transport phenomena inside the bulk material (i.e., trap filling/de-filling at grain boundaries etc), the detailed study of which remains outside the scope of this paper.

The temperature dependence of parameters R_c and C_c are more complicated. Figure 7 and its inset show the semi-log plots of these two parameters for both the dark and the LB data as a function of inverse temperature. Two regimes are identified, as shown by dotted lines. In the range 320 K > T > 250 K, R_c has an approximate activation energy of 0.21 eV under light bias, and 0.26 eV under no light bias. At temperatures below ≈ 250 K, both data sets show a much weaker temperature dependence with activation energies ranging from 74 meV to 110 meV. The inset in Fig. 7 plots the extracted fit parameter, C_c, as a function of inverse temperature for both sets of measurements, and also reveals two separate domains with different activation energies. A prior study suggests that charge injection in CdTe solar cells is dominated by the process of diffusion-limited thermionic emission [43], which in the low voltage regime predicts [44] $R_c \propto (1/\mu)\exp(\varphi_b / kT)$, where μ is the charge mobility, φ_b is the Schottky barrier height at the back contact, and k is the Boltzmann constant. This theory suggests that, at least in the higher temperature range, the extracted activation energy may correspond to the size of the back-contact barrier minus the activation energy of the mobility in that region and is consistent with various reports [9,22]. The thermionic emission theory, however, cannot explain the data collected as part of the current study over all the temperature range and seems to suggest a transition from this process to a less temperature-activated process such as tunneling of charge carriers through the contact barrier. This type of behavior has been observed in data presented by other groups as well [22], but has not been discussed in any detail and so merits further investigation.

5. Conclusions

In summary, the effects of light bias and temperature on the photo-generated current outputs of CdTe solar cells were studied using the technique of modulated photocurrent spectroscopy over a broad frequency range. In order to better understand the behavior of the data, particularly the observed photocurrent phase-lead and phase-lag with respect to the excitation source, an equivalent circuit model that accounts for a back-contact barrier that limits the photocurrent collection at the metal/semiconductor contact was developed and exercised. Good fitting agreements were observed between the model predictions and the data over a broad temperature range. The comparisons between the modeled and measured data suggest that one important limiting mechanism of current collection from the device is related to charge carrier recombination at the back contact. Further quantitative analysis based on first principle physical models is needed to achieve a greater understanding of charge generation, recombination and transport in thin film solar cells.

Acknowledgement

The authors would like to thanks Dr. Howard Yoon of NIST's Physical Measurements Laboratory for useful discussions and providing calibrated reference detectors, and Professor R. Collins of the University of Toledo for providing additional CdTe samples that showed similar behavior to the results presented with our own samples. They also thank Dr. Paul Haney, and Brian Dougherty of NIST and Professor J. R. Sites of Colorado States University for useful discussions and correspondence. This work was primarily supported by the Engineering Laboratory of the National Institute of Standards and Technology.

References

[1] M.A. Green, K. Emery, Y. Hishikawa, W. Warta, E.D. Dunlop, Solar cell efficiency tables (version 39), Prog. Photovolt: Res. Appl. 20 (2012) 12–20.

[2] F.H. Seymour, V. Kaydanov, T.R. Ohno, Simulated admittance spectroscopy measurements of high concentration deep level defects in CdTe thin-film solar cells, J. Appl. Phys. 100 (2006) 033710.

[3] F.H. Seymour, V. Kaydanov, T.R. Ohno, Admittance spectroscopy characterization of deep electronic states in cadmium telluride solar cells, Photovoltaic Energy Conversion, Conference Record of the 2006 IEEE 4th World Conference. 1 (2006) 538–541.

[4] Y.Y. Proskuryakov, K. Durose, M.K. Al Turkestani, I. Mora-Seró, G. Garcia-Belmonte, F. Fabregat-Santiago, et al., Impedance spectroscopy of thin-film CdTe/CdS solar cells under varied illumination, J. Appl. Phys. 106 (2009) 044507.

[5] Y.Y. Proskuryakov, K. Durose, B.M. Taele, G.P. Welch, S. Oelting, Admittance spectroscopy of CdTe/CdS solar cells subjected to varied nitric-phosphoric etching conditions, J. Appl. Phys. 101 (2007) 014505.

[6] Y.Y. Proskuryakov, K. Durose, B.M. Taele, S. Oelting, Impedance spectroscopy of unetched CdTe/CdS solar cells—equivalent circuit analysis, J. Appl. Phys. 102 (2007) 024504.

[7] M. Burgelman, P. Nollet, Admittance spectroscopy of thin film solar cells, Solid State Ionics. 176 (2005) 2171–2175.

[8] M.A. Lourenc, Deep level transient spectroscopy of CdS / CdTe thin film solar cells, J. Appl. Phys. 82 (1997) 1423–1426.

[9] J.V. Li, S.W. Johnston, X. Li, D.S. Albin, T. a. Gessert, D.H. Levi, Discussion of some “trap signatures” observed by admittance spectroscopy in CdTe thin-film solar cells, J. Appl. Phys. 108 (2010) 064501.

[10] A.E. Rakhshani, Heterojunction properties of electrodeposited CdTe/CdS solar cells, J. Appl. Phys. 90 (2001) 4265–4271.

[11] S.S. Hegedus, B.E. McCandless, CdTe contacts for CdTe/CdS solar cells: effect of Cu thickness, surface preparation and recontacting on device performance and stability, Solar Energy Materials & Solar Cells. 88 (2005) 75–95.

[12] A. Niemegeers, M. Burgelman, Effects of the Au/CdTe back contact on IV and CV characteristics of Au/CdTe/CdS/TCO solar cells, J. Appl. Phys. 81 (1997) 2881–2886.

[13] T.O. Kamoto, A.Y. Amada, M.K. Onagai, Characterization of Highly Efficient CdTe Thin Film Solar Cells by the Capacitance – Voltage Profiling Technique, Jpn. J. Appl. Phys. 39 (2000) 2587–2588.

[14] S. Hegedus, D. Ryan, K. Dobson, B. McCandless, D. Desai, Photoconductive CdS: how does it affect CdTe/CdS solar cell performance?, Mater. Res. Soc. Symp. Proc. 763 (2003) 1–6.

[15] M. Gloeckler, J.R. Sites, Apparent quantum efficiency effects in CdTe solar cells, J. Appl. Phys. 95 (2004) 4438–4445.

[16] R.A. Enzenroth, T. Takamiya, K.L. Barth, W.S. Sampath, Photocapacitance study of deep levels in thin CdTe PV devices, Thin Solid Films. 515 (2007) 6155–6159.

[17] A. Fahrenbruch, Current Transients in CdS/CdTe Solar Cells, Mater. Res. Soc. Symp. Proc. 865 (2005) 1–6.

[18] J.V. Li, A.F. Halverson, O.V. Sulima, S. Bansal, J.M. Burst, T.M. Barnes, et al., Theoretical analysis of effects of deep level, back contact, and absorber thickness on capacitance–voltage profiling of CdTe thin-film solar cells, Solar Energy Materials & Solar Cells. 100 (2012) 126–131.

[19] T. Eisenbarth, T. Unold, R. Caballero, C. a. Kaufmann, H.-W. Schock, Interpretation of admittance, capacitance-voltage, and current-voltage signatures in Cu(In,Ga)Se[sub 2] thin film solar cells, J. Appl. Phys. 107 (2010) 034509.

[20] S.S. Hegedus, W.N. Shafarman, Thin-film solar cells: device measurements and analysis, Prog. Photovolt: Res. Appl. 12 (2004) 155–176.

[21] S.H. Demtsu, J.R. Sites, Effect of back-contact barrier on thin-film CdTe solar cells, Thin Solid Films. 510 (2006) 320–324.

[22] G.T. Koishiyev, J.R. Sites, S.S. Kulkarni, N.G. Dhere, Determination of back contact barrier height in Cu(In,Ga)(Se,S)2 and CdTe solar cells, 2008 33rd IEEE Photovolatic Specialists Conference. (2008) 1–3.

[23] R. Bruggemann, J.P. Kleider, Photoconductivity techniques for defect spectroscopy of photovoltaic materials, Thin Solid Films. 404 (2002) 30–33.

[24] R. Herberholz, T. Walter, H.W. Schock, Density of states in CuIn(SSe)2 thin films from modulated photocurrent measurements, J. Appl. Phys. 76 (1994) 2904–2911.

[25] N. Kavasoglu, a. Sertap Kavasoglu, O. Birgi, S. Oktik, Intensity modulated short circuit current spectroscopy for solar cells, Solar Energy Materials and Solar Cells. 95 (2011) 727–730.

[26] J.P. Kleider, C. Longeaud, M.E. Gueunier, Investigation of bandgap states using the modulated photocurrent technique in both high and low frequency regimes, J. Non-Cryst. Solids. 338-340 (2004) 390–399.

[27] A. Krysztopa, M. Igalson, P. Zabierowski, J. Larsen, Y. Aida, S. Siebentritt, et al., Defect levels in CuGaSe2 by modulated photocurrent spectroscopy, Thin Solid Films. 519 (2011) 7308–7311.

[28] M. Pomoni, A. Giannopoulou, P. Kounavis, The role of the recombination centers on the modulated photocurrent: Determination of the gap state parameters of semiconductors, Phil. Mag. 90 (2010) 3441–3461.

[29] E. Ponomarev, L.M. Peter, A generalized theory of intensity modulated photocurrent spectroscopy (IMPS), J. Electroanal. Chem. 396 (1995) 219–226.

[30] J. Serhan, Z. Djebbour, a. Migan-Dubois, a. Darga, D. Mencaraglia, N. Barreau, et al., Sub-Gap Modulated Photo Current Spectroscopy performed on Cu(Inx,Ga1−x)(Sey,S1−y)2 based solar cells, Thin Solid Films. 517 (2009) 2256–2259.

[31] J. Serhan, Z. Djebbour, D. Mencaraglia, F. Couzinié-Devy, N. Barreau, J. Kessler, Influence of Ga content on defects in CuInxGa1−xSe2 based solar cell absorbers investigated by sub gap modulated photocurrent and admittance spectroscopy, Thin Solid Films. 519 (2011) 7312–7316.

[32] B.E. McCandless, S.S. Hegedus, R.W. Birkmire, D. Cunningham, Correlation of surface phases with electrical behavior in thin-film CdTe devices, Thin Solid Films. 431-432 (2003) 249–256.

[33] L. Dloczik, O. Ileperuma, I. Lauermann, Dynamic response of dye-sensitized nanocrystalline solar cells: Characterization by intensity-modulated photocurrent spectroscopy, J. Phys. Chem. B. 101 (1997) 10281–10289.

[34] J.C. Byers, S. Ballantyne, K. Rodionov, A. Mann, O. Semenikhin, Mechanism of recombination losses in bulk heterojunction P3HT:PCBM solar cells studied using intensity modulated photocurrent spectroscopy., ACS Appl. Mater. Interfaces. 3 (2011) 392–401.

[35] O.A. Semenikhin, V.E. Kazarinov, L. Jiang, K. Hashimoto, A. Fujishima, Suppression of Surface Recombination on TiO 2 Anatase Photocatalysts in Aqueous Solutions Containing Alcohol, Langmuir. 97 (1999) 3731–3737.

[36] P. Kounavis, Analysis of the modulated photocurrent experiment, Phys. Rev. B. 64 (2001) 045204.

[37] P. Dicarmine, O. Semenikhin, Intensity modulated photocurrent spectroscopy (IMPS) of solid-state polybithiophene-based solar cells, Electrochimica Acta. 53 (2008) 3744–3754.

[38] T. Oekermann, D. Schlettwein, N.I. Jaeger, Charge Transfer and Recombination Kinetics at Electrodes of Molecular Semiconductors Investigated by Intensity Modulated Photocurrent Spectroscopy, J. Phys. Chem. B. 105 (2001) 9524–9532.

[39] C.N. Kenyon, G.N. Ryba, N.S. Lewis, Analysis of Time-Resolved Photocurrent Transients at Semiconductor/Liquid Interfaces, J. Phys. Chem. 97 (1993) 12928–12936.

[40] J. Sites, J. Pan, Strategies to increase CdTe solar-cell voltage, Thin Solid Films. 515 (2007) 6099–6102.

[41] I. Visoly-Fisher, S.R. Cohen, D. Cahen, Direct evidence for grain-boundary depletion in polycrystalline CdTe from nanoscale-resolved measurements, Appl. Phys. Lett. 82 (2003) 556–558.

[42] G. Ottaviani, C. Canali, C. Jacoboni, A. Alberigi Quaranta, K. Zanio, Hole mobility and Poole-Frenkel effect in CdTe, J. Appl. Phys. 44 (1973) 360–371.

[43] C.R. Corwine, A.O. Pudov, M. Gloeckler, S.H. Demtsu, J.R. Sites, Copper inclusion and migration from the back contact in CdTe solar cells, Solar Energy Materials & Solar Cells. 82 (2004) 481–489.

[44] J.G. Simmons, Richardson-Schottky effect in solids, Phys. Rev. Lett. 15 (1965) 967–968.

Light bias current (μA)	C_d (F)	R_p (kΩ)	C_c (F)	R_c (kΩ)	R_s (Ω)	I_0 (A)	Area (mm^2)
Figure 1 device							
No LB	3.4×10^{-10}	400	1.924×10^{-9}	12.72	266	0.32	4.36
5	3.4×10^{-10}	64.8	2.47×10^{-9}	4.5	182	0.32	4.36
10	3.4×10^{-10}	30.6	2.918×10^{-9}	3.15	188	0.32	4.36
25	3.4×10^{-10}	19.5	3.324×10^{-9}	2.6	177	0.32	4.36
100	3.4×10^{-10}	7.42	4.444×10^{-9}	1.0	125	0.32	4.36
400	3.4×10^{-10}	5.32	5.48×10^{-9}	0.702	104	0.32	4.36
Figure 2 device							
No	7.1×10^{-10}	64.3	1.42×10^{-9}	25.55	83	0.385	9.0
10	7.1×10^{-10}	33.6	1.434×10^{-9}	16.5	88	0.385	9.0
30	7.1×10^{-10}	30.6	1.406×10^{-9}	18.15	151	0.385	9.0
100	7.1×10^{-10}	19	1.21×10^{-9}	15.55	167	0.385	9.0
200	7.1×10^{-10}	11	1.028×10^{-9}	10.65	308	0.385	9.0

Table 1. Parameter used in equation 2 to produce the fits shown in Figures 1 and 2.

T (K)	C_d (F)	R_p (MΩ)	C_c (F)	R_c (kΩ)	C_b (F)	R_s (kΩ)	R_{ss} (Ω)
With Light Bias							
320*	7.2×10^{-10}	0.100	5.598×10^{-9}	21.4	-	0.120	-
300*	7.2×10^{-10}	0.088	3.89×10^{-9}	28.7	-	0.156	-
280*	6.8×10^{-10}	0.111	2.102×10^{-9}	61.7	-	0.203	-
250*	6.8×10^{-10}	0.0975	2.71×10^{-9}	62.5	-	0.334	-
220*	6.8×10^{-10}	0.1005	2.71×10^{-9}	87.2	-	0.696	-
190**	6.8×10^{-10}	0.178	1.527×10^{-9}	233	3.77×10^{-10}	2.05	10
160**	6.8×10^{-10}	0.390	6.85×10^{-10}	1050	4.40×10^{-10}	8.40	2680
130**	6.8×10^{-10}	0.810	2.482×10^{-10}	4710	2.06×10^{-10}	73.6	5210
100**	6.8×10^{-10}	1.5	6.346×10^{-11}	28300	2.01×10^{-10}	524	90200
No Light Bias							
320*	7.2×10^{-10}	0.720	4.686×10^{-9}	15.6	-	0.151	-
300*	7.2×10^{-10}	0.189	2.9×10^{-9}	24.0	-	0.130	-
280*	6.8×10^{-10}	0.156	2.102×10^{-9}	31.4	-	0.198	-
250**	6.8×10^{-10}	1.362	6.088×10^{-9}	224	1.235×10^{-8}	4.63	253
220**	6.8×10^{-10}	1.38	6.594×10^{-9}	280	1.160×10^{-8}	1.64	541
190**	6.8×10^{-10}	2.48	3.418×10^{-9}	840	2.57×10^{-9}	3.30	1040
160**	6.8×10^{-10}	2.9	2.201×10^{-9}	1440	8.2×10^{-10}	15.4	1720
130**	6.8×10^{-10}	5.72	8.49×10^{-10}	5200	4.49×10^{-10}	84.0	3840

* Fit parameters obtained from equivalent circuit model 1

** Fit parameters obtained from equivalent circuit model 2

Table 2. Parameters used to produce the fits shown in figures 4 and 5. The value of I_0 used for both devices at all temperatures is 0.38 A. The device area is ≈ 9.0 mm^2.

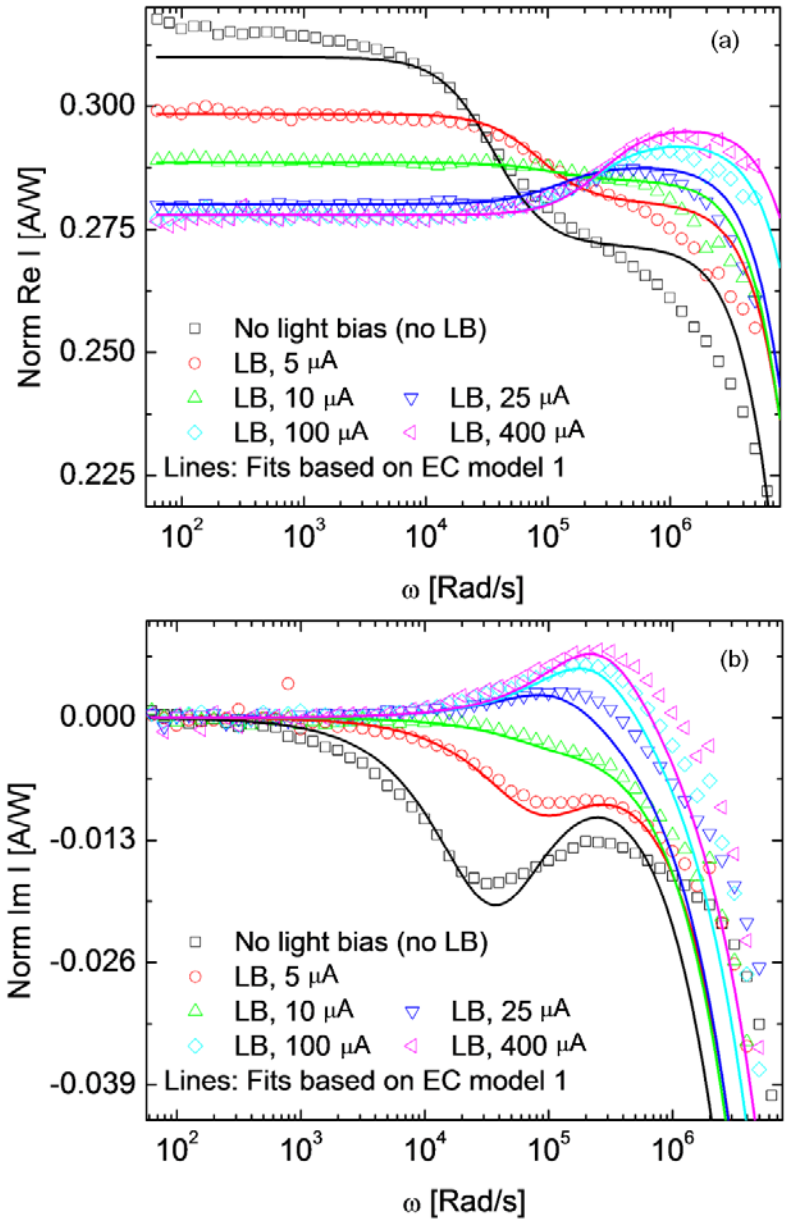

Fig. 1. The room temperature, intensity normalized real part (a), and the imaginary part (b) of the photocurrent data as a function of angular frequency for a device with reasonably good contact properties. The lines are fit to the data based on the equivalent circuit model 1 (see Fig 3b). A bias voltage of -0.2 V was maintained across the cell for all light bias curves.

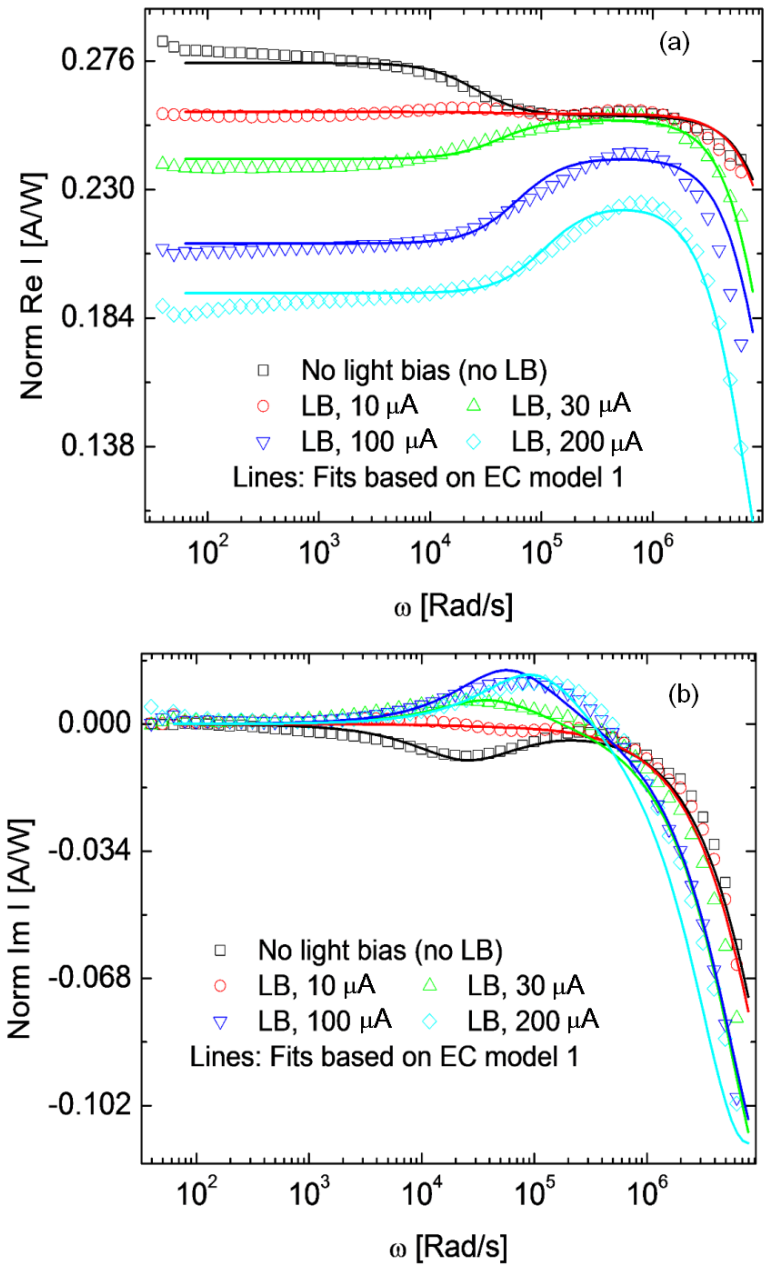

Fig. 2. The room temperature, intensity normalized real part (a), and the imaginary part (b) of the photocurrent data as a function of angular frequency for a device with poor contact properties. The lines are fit to the data based on the equivalent circuit model 1 (see Fig 3b). A bias voltage of -0.4 V was maintained across the cell for all light bias curves.

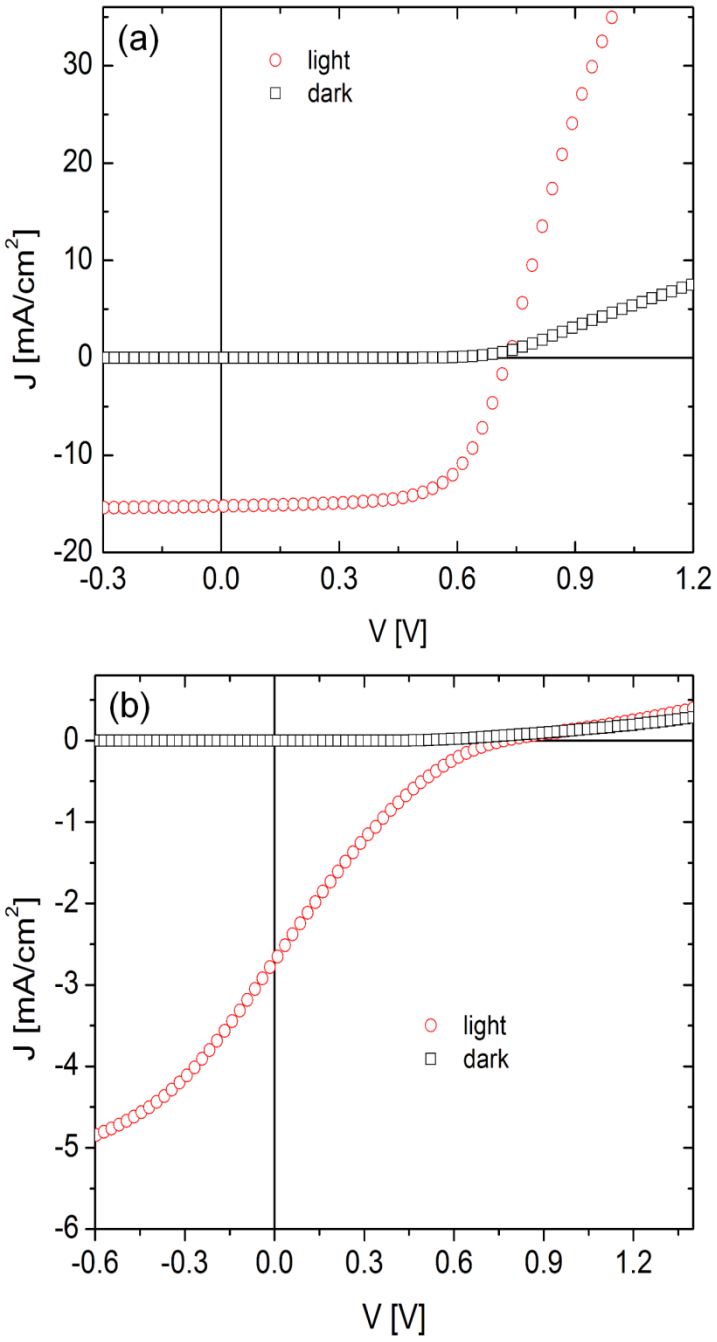

Fig. 3. (a) The dark and light current density vs. voltage characteristics for the MPCS data of Figure 1. (b) The *J-V* for the MPCS data of Figure 2. The light source for the light *J-V* was from a dc-operated LED. The LED intensities for the two measurements were not the same.

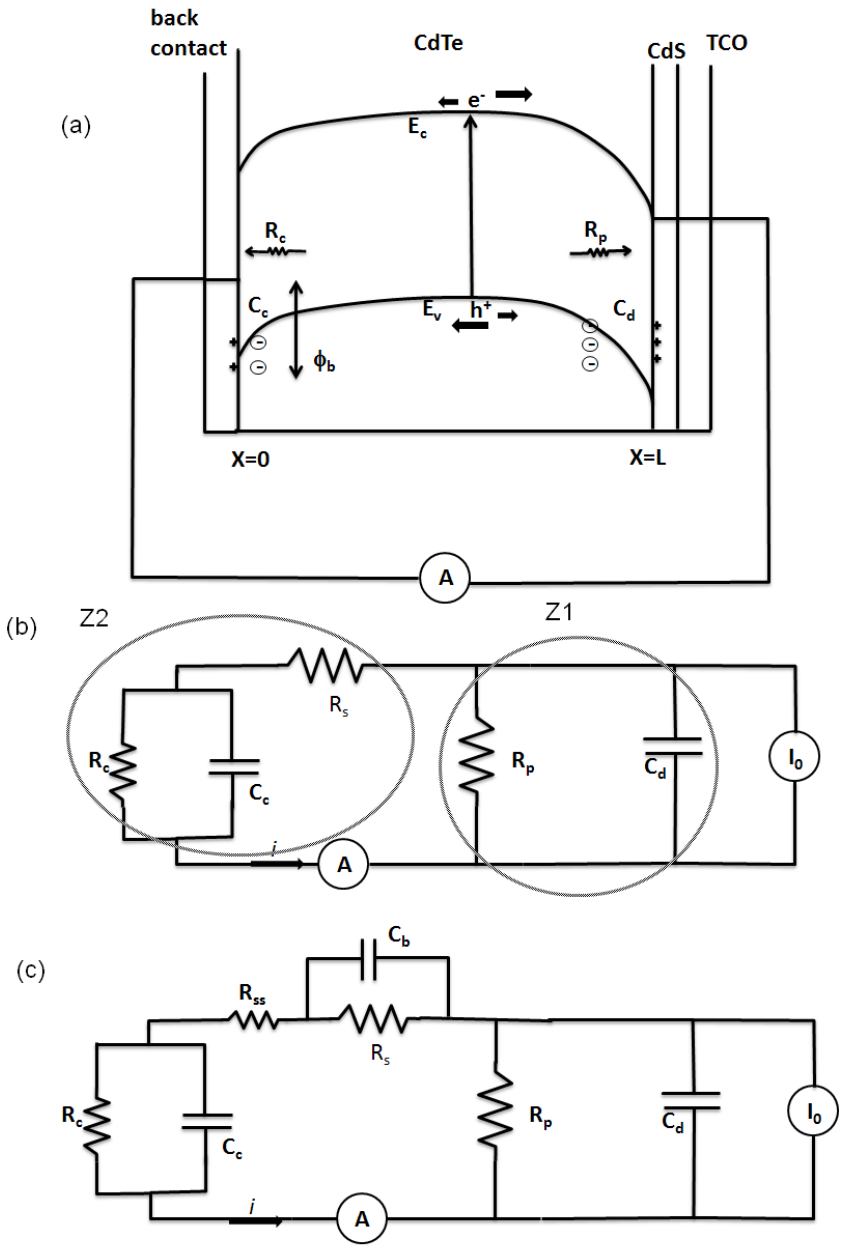

Fig. 4. (a) A simplified schematic of the energy band diagram for a CdTe device showing the junction and back contact band bending and the physical nature of various parameters associated with the equivalent circuit models. (b) The equivalent circuit model 1 used to fit the room temperature or near room temperature photocurrent data (c) A modified EC model used for low temperature fitting of the photocurrent data.

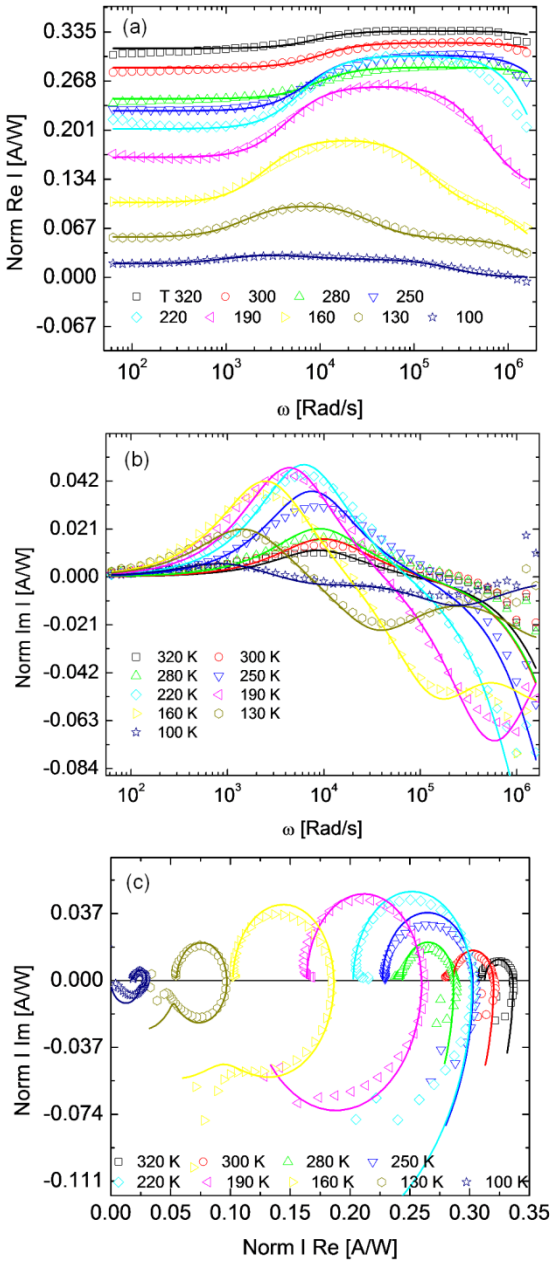

Fig. 5. The temperature dependence of the intensity-normalized real part vs. ω (a), the imaginary part vs. ω (b) and the Nyquist real vs. imaginary components of the photocurrent data for a contact-limited CdTe solar cell under light bias (c). The lines are fit to the data based on the equivalent circuit models 1 (320 K to 220 K), and model 2 (190 K to 100 K).

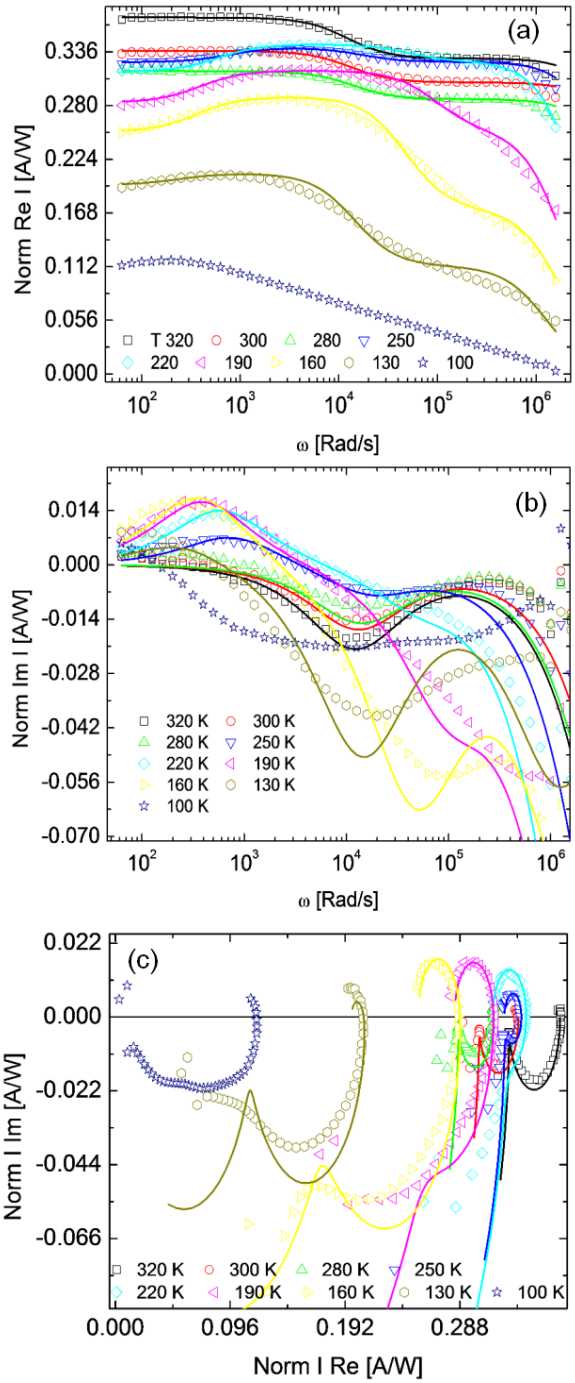

Fig. 6. The temperature dependence of the intensity-normalized real part vs. ω (a), the imaginary part vs. ω (b) and the Nyquist real vs. imaginary components of the photocurrent data for a contact-limited CdTe solar cell under no light bias (dark background) (c). The lines are fit to the data based on the equivalent circuit models 1 (320 K to 280 K), and model 2 (250 K to 130 K)

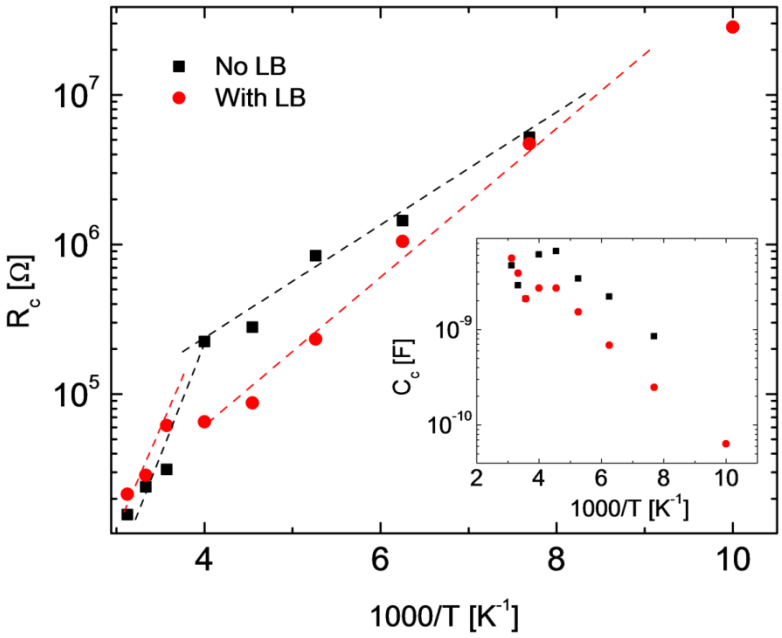

Fig. 7. (inset) Semi-log plot of the fit parameter, C_c, as a function of inverse temperature. (main) Semi-log plots of the fitted contact resistance parameter, R_c, as a function of inverse temperature, showing two separate temperature regimes with different activation energies.